A&A 487, 247–252 (2008)
DOI: 10.1051/0004-6361:200809577

Astronomy & Astrophysics

CN Zeeman measurements in star formation regions

E. Falgarone[1], T. H. Troland[2], R. M. Crutcher[3], and G. Paubert[4]

[1] LERMA/LRA, CNRS UMR 8112, École Normale Supérieure and Observatoire de Paris, 24 rue Lhomond, 75231 Paris Cedex 05, France
e-mail: edith@lra.ens.fr
[2] University of Kentucky, Department of Physics and Astronomy, Lexington, KY 40506, USA
e-mail: troland@pa.uky.edu
[3] University of Illinois, Department of Astronomy, Urbana, IL 61801, USA
e-mail: crutcher@uiuc.edu
[4] IRAM, 7 avenida Divina Pastora, Granada, Spain
e-mail: paubert@iram.es

Received 14 February 2008 / Accepted 17 May 2008

ABSTRACT

Aims. Magnetic fields play a primordial role in the star formation process. The Zeeman effect on the CN radical lines is one of the few methods of measuring magnetic fields in the dense gas of star formation regions.
Methods. We report new observations of the Zeeman effect on seven hyperfine CN $N = 1-0$ lines in the direction of 14 regions of star formation.
Results. We have improved the sensitivity of previous detections, and obtained five new detections. Good upper limits are also achieved. The probability distribution of the line-of-sight field intensity, including non-detections, provides a median value of the total field $B_{\rm tot} = 0.56$ mG while the average density of the medium sampled is $n(H_2) = 4.5 \times 10^5 {\rm cm}^{-3}$. We show that the CN line probably samples regions similar to those traced by CS and that the magnetic field observed mostly pervades the dense cores. The dense cores are found to be critical to slightly supercritical with a mean mass-to-flux ratio $M/\Phi \sim 1$ to 4 with respect to critical. Their turbulent and magnetic energies are in approximate equipartition.

Key words. magnetic fields – stars: formation – ISM: molecules – turbulence – polarization – ISM: kinematics and dynamics

1. Introduction

The role of magnetic fields in the formation of structure in dense molecular clouds and in the star formation process remains unclear (see Crutcher 2007, for a recent review). If sufficiently strong, magnetic fields may support clouds against gravitational collapse and thus prevent or delay star formation. Shu et al. (1999), Mouschovias & Ciolek (1999), and MacLow & Klessen (2004) have reviewed the theory. Magnetic fields appear to provide the only viable mechanism for transporting angular momentum from collapsing cores, and they may play a significant role in the physics of bipolar outflows and jets that accompany protostar formation (Cabrit 2007). Observation of magnetic fields in molecular clouds is therefore crucial.

Crutcher (2007) reviewed the various techniques and results for studying magnetic fields in molecular clouds. Of these techniques, the Zeeman effect provides the only direct method for measuring magnetic field strengths in molecular clouds. To date, detections of the Zeeman effect in the interstellar medium have been made only in lines of H I, OH, CN, and H_2O. Thermal lines of the first two species probe relatively low-density gas – $n({\rm H}) < 10^4$ cm^{-3}. OH and H_2O maser emission lines probe high densities, but in special regions – very localized in space and perhaps shock compressed. As a tracer of high density gas, the CN thermal lines probe dense regions in molecular clouds and CN Zeeman observations are therefore a unique tool for measuring magnetic field strengths in star formation regions.

The radio transitions of CN have been discussed extensively by Turner & Gammon (1975). The Einstein A of the strongest CN hyperfine component within the $\lambda = 3$ mm $N = 1 \rightarrow 0$ transition is $A = 1.19 \times 10^{-5}$ s^{-1}, which means that the $N = 1 \rightarrow 0$ transition of CN offers the opportunity to measure magnetic fields in the density range 10^4 to 10^6 cm^{-3}, the density of molecular cores that may be in transition from equilibrium (between gravity and magnetic/turbulent support) to collapse to form stars.

Previously, a successful series of CN Zeeman observations was carried out with the IRAM 30-m telescope, with a quarter-wave plate polarimeter (Crutcher et al. 1996, 1999). In this paper we report additional results obtained with the IRAM-30 m telescope with a new correlation spectropolarimeter. We both improved the sensitivity of some of the previous results and obtained data on new sources.

2. The CN Zeeman effect

Table 1 lists the 7 strongest CN hyperfine lines together with each line's frequency, relative intensity, Zeeman splitting coefficient, and relative sensitivity to the Zeeman effect (the product of the Zeeman splitting coefficient and the relative intensity). The fact that the $N = 1 \rightarrow 0$ transition of CN has 7 strong hyperfine components (there are actually 9 components, but 2 are much weaker than the others and hence are not useful for Zeeman observations) with very different Zeeman splitting factors is essential for the success of CN Zeeman measurements.

Table 1. CN $N = 1-0$ hyperfine lines.

Line	ν (GHz)	RI[a]	Z (Hz/μG)[b]	RI $\times$ Z[c]
1	113.144	8	2.18	17.4
2	113.171	8	–0.31	2.5
3	113.191	10	0.62	6.2
4	113.488	10	2.18	21.8
5	113.491	27	0.56	15.1
6	113.500	8	0.62	5.0
7	113.509	8	1.62	13.0

[a] RI is the relative intensity of each hyperfine component.
[b] Z is the Zeeman splitting factor of each hyperfine component.
[c] RI $\times$ Z is the relative sensitivity to $B_{\rm los}$.

Instrumental polarization such as beam squint (a two-lobe pattern in the circularly polarized primary telescope beam), polarized sidelobes, et cetera will typically produce a Stokes V signal in the CN spectra that is comparable to or larger than the Zeeman signal. There is no way to avoid this for extended emission, and it would be extremely difficult, if not impossible, to eliminate these instrumental polarization artifacts. The main effect of instrumental polarization is to produce a pseudo-splitting of the spectral line that appears to mimic Zeeman splitting. However, instrumental polarization does not know about the Zeeman effect. The CN Zeeman splitting factor (Crutcher et al. 1996) varies quite significantly among the 7 hyperfine components (see Table 1). It is possible to observe all 7 hyperfine lines simultaneously and to fit the 7 observed Stokes V spectra to the expression: $V_i(v) = C_1 I_i(v) + C_2 \frac{dI_i(v)}{dv} + C_3 Z_i \frac{dI_i(v)}{dv}$, where $i = 1$ to 7 for the 7 hyperfine components and Z_i is the Zeeman splitting factor for each hyperfine line. C_1 absorbs any gain difference between left and right polarization and any linearly polarized line signal. C_2 absorbs any instrumental polarization effects that produce pseudo-Zeeman splitting. C_3 is non-zero only if there is circular polarization line splitting due to the CN Zeeman effect. Crutcher et al. (1996) tested this fitting procedure with simulated noisy data and found that it is robust; for example, a 2σ Zeeman signal can be reliably extracted from data with more than an order of magnitude larger instrumental polarization artifacts. For CN Zeeman observations the polarimeter need not be perfect (as indeed the quarter-wave plates used previously were definitely not), and polarized sidelobes that would severely affect attempts to measure polarization of extended emission or other instrumental polarization effects do not prevent success.

3. Observations

Observations were carried out with the IRAM-3 0m telescope, which has a beam width of 23″ at this frequency, in May 2004, 2005, 2006 and 2007. In order to observe at the peak CN line positions, we first made very short Stokes I maps (generally 5-point maps). For our observations the two orthogonally polarized heterodyne receivers were made coherent by sharing reference synthesizers. The signals from the receivers were fed to the Vespa correlator which performed the auto-correlations and cross-correlations of the signals from both receivers. This gave 4 spectra – the power spectra of the horizontally and vertically (in the receiver cabin) polarized receivers, and the real and imaginary parts of the cross-correlations (i.e., the horizontally polarized receiver correlated with the vertically polarized receiver).

The spectra were first converted to temperature scale by applying the standard calibration procedure for spectral observations. The next step was to correct for the phase errors: while the receivers are coherent, they exhibit an unknown phase difference (due to slightly different optical paths, unmatched cable lengths, absolute phase of the spectrometers) which must be taken into account. This difference was measured by taking an additional spectrum on a cold load through a polarization grid during the calibration procedure. The uncertainty on the phase correction in each individual channel was about 0.1° rms. It was also very stable with time, varying by less than 1° per hour.

The phase correction was applied to the cross-correlation spectra to obtain 4 spectra in the receiver cabin domain (Horizontal, Vertical, Real and Imaginary). Stokes I is Horizontal+Vertical and the imaginary part of the cross-correlation spectra is Stokes V, the circular polarization component. We therefore obtained Stokes I and V spectra for each source. Although Stokes U and Q spectra were potentially available, we did not make use of these data.

4. Results

Together with the earlier CN Zeeman observations, there are now sensitive CN Zeeman observations toward 14 positions. CN Zeeman results for OMC1n4 are from Crutcher et al. (1996) and for OMC1s, DR21OH1, and DR21OH2 are from Crutcher et al. (1999). Results for other positions are based on the observations reported here, both of new sources and additional integrations on previously observed positions to improve the sensitivity.

Table 2 gives positions and various physical parameters for the CN Zeeman sources. Appendix A gives additional notes on the individual clouds, including especially the references for the density and radius of each. $T_{\rm A}^*$ is the observed line strength of the strongest hyperfine component, line 5 in Table 1. v is the line peak velocity with respect to the local standard of rest, and Δv is the full line width at half maximum intensity. Distances (d) are taken from the literature. The radius of the CN sources we observe (r) are determined from the distances and the measured angular sizes of CN emission if available, or other tracers such as CS if not. We assumed that CN and the other high density tracers are co-located, although only higher angular resolution (interferometer) mapping can test this assumption.

Simon (1998) mapped many of the CN Zeeman clouds with the IRAM-30 m telescope in both the CN $N = 1 \rightarrow 0$ and $N = 2 \rightarrow 1$ lines; we determine radii from his maps whenever possible. The volume densities of H_2 in the regions where CN is observed are taken from the literature, usually from analysis of the excitation of CS lines; the critical density of the $J = 2 \rightarrow 1$ CS transition is $n \approx 8 \times 10^4$ cm^{-3}, very similar to that of the $N = 1 \rightarrow 0$ CN transition (Turner & Gammon 1975) (see Appendix A for details).

The column density of H_2 has been estimated in two ways. (1) $N_{n,r}(H_2)$ comes from $n(H_2)$ and the core radius, assuming a spherical core. (2) $N_{\rm CN}(H_2)$ comes from our inference of the column density of CN molecules, as follows. Our spectra show that although the measured relative intensities of the 7 hyperfine components vary slightly from their optically thin LTE ratios (Table 1), the variations are not large, suggesting that the CN lines are optically thin. We checked this quantitatively as follows. We assumed LTE, which implies that, except for line optical depth effects, the relative strengths of the observed lines should be those given in Table 1. Lines 3 and 4 have the same relative intensity, so we averaged these observed line strengths and obtained the observed strength of relative intensity 10 lines from this average. We then computed the ratio of the observed strengths of line 5 to the line 3 and 4 average. For a very large

Table 2. CN Zeeman sources – positions and physical parameters.

Cloud	α(2000)	δ(2000)	T_A^* K	v km s^{-1}	Δv km s^{-1}	d kpc	r pc	$n(H_2)$ 10^5 cm^{-3}	$N_{n,r}(H_2)$ 10^{23} cm^{-2}	$N_{CN}(H_2)$ 10^{23} cm^{-2}	M_{obs} $M_\odot$	M_{vir} $M_\odot$
W3OH	02 27 04.1	61 52 22	2.2	–46.5	4.2	2.4	0.12	1.5	1.1	0.9	88	430
OMC1s	05 35 13.5	–05 22 52	14.7	8.5	2.0	0.45	0.03	18	3.4	2.3	17	26
OMC1n1	05 35 14.5	–05 22 07	13.0	9.9	1.4	0.45	0.03	18	3.6	1.5	16	13
OMC1n4	05 35 16.8	–05 19 31	14.5	9.4	1.5	0.45	0.03	14	2.8	2.2	18	15
NGC2024	05 41 44.2	–01 55 41	8.6	11.0	2.2	0.45	0.04	5.9	1.4	2.2	18	40
S255	06 12 53.7	17 59 22	5.6	7.3	2.3	2.5	0.18	3.7	4.2	1.3	500	200
G10.6	18 10 28.7	–19 55 49	8.9	2.8	5.8	6.5	0.19	14	16.4	4.9	2100	1300
M17SWHI	18 20 22.9	–16 11 32	17.3	19.9	4.3	1.3	0.11	6.0	4.2	6.2	430	440
M17SWCN	18 20 25.0	–16 13 42	16.9	19.6	3.3	1.3	0.10	6.0	3.7	5.3	290	230
S106OH	20 27 28.4	37 22 41	5.3	–1.7	2.0	1.7	0.07	1.0	0.4	0.9	17	55
S106CN	20 27 29.5	37 22 54	7.3	–1.8	1.9	1.7	0.07	1.0	0.4	1.3	21	50
DR21OH1	20 38 59.9	42 22 38	4.5	–4.7	2.3	3	0.15	1.7	1.5	1.0	170	160
DR21OH2	20 38 59.9	42 22 38	2.6	–0.9	2.3	3	0.15	1.7	1.5	0.7	140	160
S140	22 19 17.1	63 18 35	6.0	–6.3	2.4	0.9	0.05	6.0	1.0	1.3	28	63

line optical depth, this ratio should be 1; for a very small line optical depth, the ratio will be 2.7. All but one of these ratios are within the range 2.7–1 expected for LTE line strengths and zero to infinite line optical depth; the one that is not has the RI = 10 lines only very slightly too weak for LTE and low optical depth. The maximum line optical depth found by this technique is $\tau \approx 0.5$. We therefore compute the column density in the $N = 0$ state assuming the RI = 10 lines are optically thin (see Turner & Gammon 1975). We then compute the total column density of CN in all states by assuming that all states are excited with an assumed excitation temperature of 25 K. (These are warm, dense cores, and several of the T_A^* are not too far below 25 K in strength.) We then assume $CN/H_2 = 4 \times 10^{-9}$ in order to find $N_{CN}(H_2)$. This value of CN/H_2 is consistent with those found by Turner & Gammon (1975) in dense, warm cores, and matches the results found in OMC1 cores by Johnstone et al. (2003). Finally, we compute the observed masses M_{obs} of the CN Zeeman sources from the radii and geometric mean of $N_{n,r}(H_2)$ and $N_{CN}(H_2)$, denoted $N_{23}(H_2)$ in the following. We also list for comparison the virial masses $M_{vir} = 210 r \Delta v^2\ M_\odot$, where r is expressed in pc and Δv in km s^{-1}.

As an example of the data, Fig. 1 shows the spectra of W3OH. The Stokes I spectrum is the average (weighted by the sensitivity to the Zeeman effect) of hyperfine lines 1, 4, 5, and 7 (Table 1); these are the lines that have significant sensitivity to the Zeeman effect. The Stokes V spectrum is the equivalent average, where the non-Zeeman contributions to the observed V due to gain imbalance and instrumental polarization (coefficients C_1 and C_2 in the fitting equation (Sect. 2)) have been removed. For W3OH the instrumental polarization contribution to Stokes V is the equivalent of a 5.6 mG Zeeman signal for a (totally artificial) $Z = 1$ Hz/μG for all 7 hyperfine components. Hence, the instrumental polarization contribution in this case is about 5 times greater than the true Zeeman signal. Only the large variation in the Zeeman splitting factors among the hyperfine components makes it possible to obtain reliable B_{los} results from CN Zeeman observations, as discussed in Sect. 2. Overplotted on Stokes V is $dI/d\nu$ computed from the average Stokes I spectrum and scaled to the fitted magnetic field strength, $B_{los} = +1.10$ mG.

In Table 3, we list the line-of-sight magnetic field strength B_{los} and the 1σ uncertainty in each measurement. Instrumental polarization effects have been eliminated from the Stokes V spectra by the fitting procedure, so the uncertainty in each measurement is dominated by stochastic noise. Earlier during the series of CN Zeeman observations (Crutcher et al. 1996)

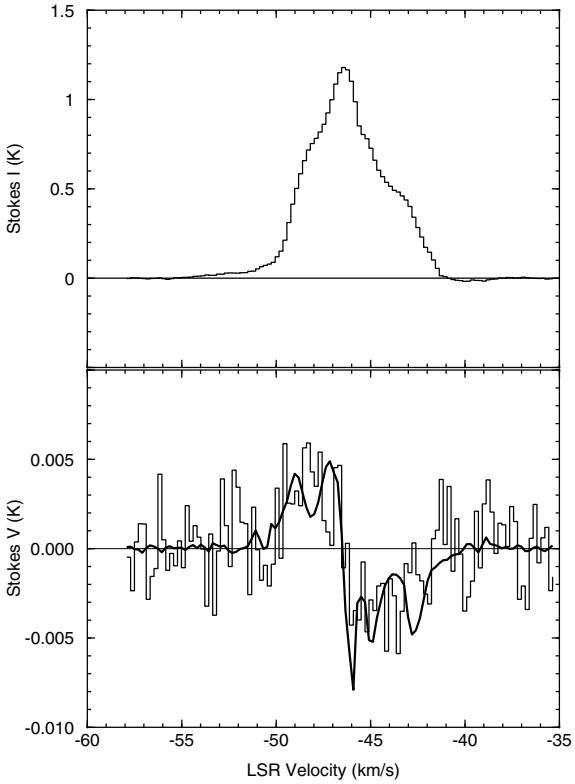

Fig. 1. W3OH CN Zeeman spectra. The top plot is the Stokes parameter I spectrum, and the bottom plot is the Stokes parameter V spectrum (histogram) and $dI/d\nu$ (heavy line) scaled for $B_{los} = +1.10$ mG.

we tested the Zeeman fitting procedure by simulating the fitting process with artificially generated spectral lines with various B_{los} and random spectral noise. We then fitted the resulting spectra to test what signal-to-noise ratio was required to achieve a reliable detection of B_{los}. We found that the results followed the normal probability distribution function, so at the 2σ level 4.6% of the measurements would be false positives. For 14 measurements (the number of cloud measurements reported here), one would then expect 0.6 false "detections" of B_{los}. We therefore adopted 2σ as the statistically valid cut off for claiming detections. Our lowest signal-to-noise ratio is slightly above 2σ. Therefore, the detections we claim here are all probably real, although it is possible (although statistically unlikely) that 1 or even 2 of the

Table 3. CN Zeeman magnetic field results.

Cloud	B_{los} mG	σ mG	M/Φ (wrt critical)	$\mathcal{M}$ 10^{-9} erg cm^{-3}	$\mathcal{T}$ 10^{-9} erg cm^{-3}	$\mathcal{M}/\mathcal{T}$
W3OH	1.10	0.33	≤0.6	≥48	5.8	≥8
OMC1s	0.04	0.24	–	–	16	–
OMC1n1	–0.36	0.08	≤4.5	≥5.2	7.8	≥0.7
OMC1n4	0.08	0.10	–	–	6.9	–
NGC2024	0.01	0.12	–	–	6.3	–
S255	–0.73	0.34	≤2.2	≥21	4.3	≥5
G10.6	0.74	0.27	≤8.4	≥22	100	≥0.2
M17SWHI	0.14	0.13	–	–	24	–
M17SWCN	–0.22	0.08	≤14	≥1.9	14	≥0.1
S106OH	–0.52	0.38	–	–	0.9	–
S106CN	–0.06	0.20	–	–	0.8	–
DR21OH1	–0.36	0.10	≤2.4	≥5.2	2.0	≥2.6
DR21OH2	–0.71	0.12	≤1.0	≥20	2.0	≥10
S140	–0.25	0.09	≤4.4	≥2.5	7.6	≥0.3

results near the 2σ limit may not be true detections. There are therefore 8 probable detections of B_{los} and 6 sensitive upper limits. Finally, we list the mass-to-magnetic flux ratios M/Φ with respect to critical and the magnetic and kinetic energy densities $\mathcal{M} = B^2/8\pi$ and $\mathcal{T} = \frac{1}{3}\rho\sigma^2$. *Note that the quantities involving the magnetic field strength are determined from B_{los} and not B_{tot}.* B_{los} is a lower limit to B_{tot}; hence, for detections of the magnetic field, M/Φ is an upper limit and $\mathcal{M}$ is a lower limit, as shown in the table. For non-detections of the Zeeman effect, we have a 2σ *upper* limit on B_{los}; hence, we do not list values for the magnetic quantities in these cases.

5. Comparison with other observations

Toward S140 our result is $B_{los} = -0.25 \pm 0.09$ mG, a detection at the 2.8σ level. Uchida et al. (2001) reported no detection in SO $J_N = 1_2{-}1_1$ line Zeeman observation, with $\sigma(B_{los}) \approx 0.4$ mG, which is consistent with our result. The critical density of the SO transition is about an order of magnitude higher than that of the CN transition, so SO samples higher density gas. The CN and SO observations were at the peak line strengths positions in each species, and differed by ∼30″, or about half the SO beam width.

Toward W3OH our result is $B_{los} = +1.1 \pm 0.3$ mG, a detection at the 3.7σ level. Güsten et al. (1994) reported a Zeeman detection in their excited-state OH absorption line observations, and inferred $B_{los} = +3.2 \pm 0.6$ mG from a fit to the entire I profile. However, comparison of the results is complicated by the fact that the line profiles of OH and CN do not agree in detail. The OH line has two components, at −45.1 and −47.5 km s^{-1}. Güsten et al. felt that the Zeeman signal came from the stronger component at −45.1 km s^{-1}, and inferred $B_{los} = +3.1 \pm 0.4$ mG from a fit to that component only. The CN line appears to have three velocity components, none of which agrees precisely with the OH components. These differences may be due to the fact that the OH absorption must come from our side of the continuum, while the CN emission may come from behind the continuum. Also, CN is seen in emission with a 23″ beam, while the OH is in absorption against the ∼1″ compact H II region. Moreover, the two transitions sample different densities. The Λ-doublet lines are within the $^2\Pi_{3/2}, J = 7/2$ state of OH, which is 290 K above the ground state. The OH observations therefore sample hot, dense gas. Cesaroni & Walmsley (1991) estimated $n(H_2) \sim 7 \times 10^6$ cm^{-3} and $T_{dust} \approx 150$ K for the region probed by the excited-state OH lines.

We observed two positions toward the M17SW molecular cloud. The M17SW(CN) position is at a local CN peak intensity position. That position was also observed during the earlier experiment (Crutcher et al. 1999), when $B_{los} = -0.33 \pm 0.14$ mG was reported. That is consistent with our new result of $B_{los} = -0.16 \pm 0.10$ mG; combining the two observations yields $B_{los} = -0.22 \pm 0.08$ mG. Our results can be compared with VLA H I and OH absorption-line Zeeman maps (Brogan & Troland 2001) made with beams sizes close to our CN beam size. They did not report a detection in H I at our M17SW(CN) position, but an extrapolation from positions ∼1 beam away suggests $B_{los} \approx -0.1$ mG in the 20 km s^{-1} velocity component, in fair agreement with our result. The M17SW(HI) position corresponds to a position where $B_{los} \approx -0.5$ mG in both OH and H I. The VLA result is completely different from our CN result of $B_{los} = +0.14 \pm 0.13$ mG; although our CN result is not a detection, it differs by $\sim 5\sigma$ from the VLA results. As for W3OH, the CN emission and OH and HI absorption lines may sample different regions.

6. Discussion

6.1. Origin of the CN line emission

Our targets are peaks of CN $N = 1 \rightarrow 0$ line emission in active star formation regions. In most cases, these peaks do not exactly coincide in projection with the center of dense cores, as traced by other molecular lines such as CS and isotopes or HC_3N. This could perhaps be explained by the formation routes of CN. Boger & Sternberg (2005) suggest that in gas denser than 10^4 cm^{-3}, the entire CN column density is built up in the C^+/C/CO transition layer and the larger the density, the sharper the concentration of the regions of large CN abundances in the illuminated layers ($A_v < 2$ mag). In this astrochemical picture, the CN $N = 1 \rightarrow 0$ transition with its critical density of the order of 10^5 cm^{-3} is selectively sensitive to UV irradiated layers of dense cores, and/or dense PDRs. The CN Zeeman measurements would then sample a magnetic field strength that is not necessarily that present within the dense core itself. However, our inferrence of CN column densities seems to be at odds with this astrochemical picture.

Our analysis of the CN data yielded the CN column densities in the ground state, N_0(CN); over the 14 positions the range was 2×10^{13} cm^{-2} < N_0(CN) < 9×10^{13} cm^{-2}, with a geometric mean N_0(CN) ≈ 7×10^{13} cm^{-2}. Our LTE calculation of the column densities in all rotational states yielded

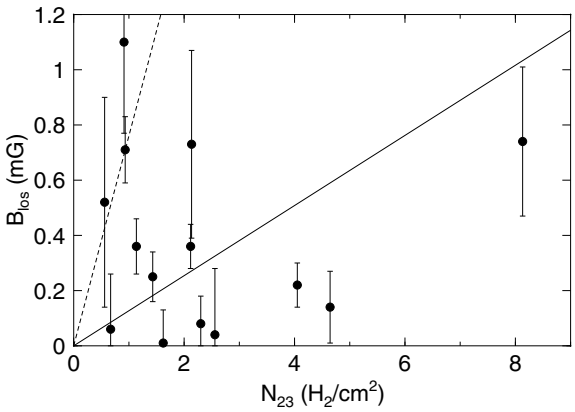

Fig. 2. The line-of-sight magnetic field strength from our CN Zeeman observations versus the column density of H_2 (the geometric mean of our two determinations). N_{23} is $N \times 10^{-23}$. The dashed line is the critical mass-to-flux ratio, and the solid line is the median mass-to-flux ratio inferred from $B_{\rm los}$ (before geometric corrections).

2×10^{14} cm^{-2} < N(CN) < 2×10^{15} cm^{-2}, with a geometric mean N(CN) $\approx 6\times10^{14}$ cm^{-2}. With [CN]/[H_2] = 4×10^{-9}, these values for N(CN) yielded $N_{\rm CN}(H_2)$ in reasonable agreement (i.e., within a factor 3) with $N_{n,r}(H_2)$, derived from volume densities and radii. This agreement suggests that the value [CN]/[H_2] we used is approximately correct. The values for N(CN) and [CN]/[H_2] do not agree with theoretical astrochemical values (cf. Boger & Sternberg 2005), which are based on CN existing in PDR regions only. In particular, the model has significantly lower N(CN) than the values we observe. Our results suggest that the CN in the regions we observe sample approximately the same regions and densities as sampled by CS, and therefore that CN serves as a good probe of magnetic field strengths in dense regions, $n(H_2) \sim 10^{5-6}$ cm^{-3}. This view may be supported by the recent findings of Hily-Blant et al. (2008) who show that CN, like N_2H^+ and unlike CO, is not depleted towards the central parts of two dense cores.

6.2. Mass to flux ratio

Figure 2 shows our measured $B_{\rm los}$ in mG versus $N_{23}(H_2)$ in 10^{23} cm^{-2}. We can use these values to compute the measured mass-to-flux ratios with respect to the critical value, $(M/\Phi)_{cr} \approx 0.76\, N_{23}(H_2)/B$(mG) (cf. Crutcher 2004). The weighted (by uncertainties in $B_{\rm los}$) mean value of the mass-to-flux ratio with respect to critical is $M/\Phi = 6.0\pm0.5$. All measurements, including the non-detections, are included in this calculation. That mean value is plotted as a solid line. The dashed line shows the locus of critical mass-to-flux ratio; points above this line would have a subcritical M/Φ. Keeping in mind that $B_{\rm los}$ is a *lower* limit to $B_{\rm tot}$, all observed points on this plot could be higher (less supercritical, more subcritical) if we could plot $B_{\rm tot}$. Two points lie on the critical line and one lies above the critical line even with $B_{\rm los}$ being plotted. This suggests that these cores are critical to subcritical, but the uncertainties in the measures of $B_{\rm los}$ are too large for a definite result.

Although we can only determine upper limits on the mass-to-flux ratios for individual sources, we can use our weighted mean value to carry out a statistical assessment. Heiles & Troland (2005) have shown that the observed distribution of $B_{\rm los}$ does constrain the median value of $B_{\rm tot}$, and that the average value of $B_{\rm los}$ is close to $B_{\rm tot}/2$ for a wide range of probability distributions of $B_{\rm tot}$. We need to correct for the facts that we measure only the line-of-sight component of the magnetic field (the factor of 1/2 correction discussed above), and that if the cores have a disk morphology we overestimate the column densities along the magnetic field (see Crutcher 2004). The combined correction for both of these geometry effects is 1/3, so our best estimate for the mean mass-to-flux ratio in these cores is $M/\Phi \approx 2.0$ with respect to critical. Hence, our determination of the mean value of M/Φ yields a slightly supercritical result. However, the estimate of column densities is uncertain by ~2, so the possible range of the mean mass-to-flux ratio is $M/\Phi \sim 1-4$, or critical to supercritical by a factor of four.

6.3. Alfvénic Mach number

The Alfvénic Mach number is given by $M_{\rm A} = \sqrt{3}\sigma/v_{\rm A}$, where σ is the one-dimensional velocity dispersion and $v_{\rm A} = B_{\rm tot}/\sqrt{4\pi\rho}$ is the Alfvén speed. Then $M_{\rm A} = 5.1\times10^{-4}\sqrt{n(H_2)}\Delta v/B_{\rm tot}$, where $n(H_2)$ is in cm^{-3}, Δv is in km s^{-1}, the total field strength $B_{\rm tot}$ is in mG, and we have assumed Gaussian velocity profiles and a 10% He abundance. The geometric mean values from Tables 2 and 3 are $n(H_2) = 4.5\times10^5$ cm^{-3}, $\Delta v = 2.5$ km s^{-1}, and $B_{\rm los} = 0.28$ mG. With the mean geometrical statistical correction $2B_{\rm los} = B_{\rm tot}$, we have a mean Alfvénic Mach number $M_{\rm A} = 1.5$. Therefore, turbulent and magnetic energies are in approximate equipartition.

7. Conclusions

These new observations of the Zeeman effect on the CN $N = 1-0$ lines have significantly improved the statistics on the magnetic field intensity in dense star formation regions. We use our 8 detections and 6 non-detections to derive a median value of the total field $B_{\rm tot} = 0.56$ mG in gas of average density $n(H_2) = 4.5\times10^5$ cm^{-3}. We show that the CN line probably samples regions similar to those traced by CS and are therefore confident that the magnetic field observed mostly pervades the dense cores. The dense cores are found to be critical to slightly supercritical with a mean mass-to-flux ratio $M/\Phi \sim 1$ to 4, with respect to critical. Their turbulent and magnetic energies are in approximate equipartition, or the observed internal motions are slightly super-Alfvénic.

Since the Zeeman effect is sensitive only to the line-of-sight component of the field, more definite results can be obtained only if the statistical sample is larger. The range of densities of interest to star formation critically requires more CN Zeeman measurements (detections and sensitive upper limits).

Acknowledgements. This work was supported in part by the National Science Foundation under NSF grants AST 0205810, 0307642, and 0606822 and PHY 0551164. This paper is preprint number NSF-KITP-07-200. We are indebted to Pierre Hily-Blant for his help in preparing procedures with the New Control System at IRAM-30 m.

Appendix A: Notes and references for individual sources

W3OH: Distance from Reid et al. (2005), radius from Kim et al. (2006); close to H II region, ~10″ from submm source (Mueller et al. 2002). Density is inferred from the observations of $C^{34}S(3-2)$ and 5–4 by Plume et al. (1997).

OMC1s, OMC1n1, OMC1n4: Radii from Simon (1998), Tatematsu et al. (1993).

NGC2024: Radius from Simon (1998); density from CS multitransition analysis of Lada et al. (1997), adopting the

mean logarithmic value of the density determined over the region emitting in CS(5-4). The CN position lies at the edge of the densest north-south ridge.

S255: Radius from Simon (1998); the CN position in S255 coincides with the dust continuum source SMM2, and the gas density is derived from this study (Minier et al. 2005).

G10.6: Radius from Ho et al. (1994); the CN position is that of the dust continuum emission peak (Mueller et al. 2002) and the density is that deduced from CS multi-transition analysis by Omodaka et al. (1992). This density is very close to that deduced from the density distribution found by Mueller et al. (2002) for that source, at half-power radius or 0.2 pc from the center.

M17SWHI, M17SWCN: The CN peak in M17SW is at the edge of the dense PDR and the H_2 density is inferred from the CS multitransition analysis of Wang et al. (1993). It is consistent with the density derived from HC_3N by Bergin et al. (1996). There is no indication, according to these tracers for a lower density at the position of M17SW(HI), 1.5′ south of M17SW(CN).

S106CN, S106OH: Radius from Simon (1998); distance from Schneider et al. (2007); density from Vallée & Fiege (2005).

DR21OH1, DR21OH2: Radius from Padin et al. (1989); density from Vallée & Fiege (2006).

S140: The CN peak (Simon 1998) is 3″ east, 5″ south of SMM1 (Minchin et al. 1995); the density is inferred from the CS multitransition analysis of Zhou et al. (2004).

References

Bergin, E. A., Snell, R. L., & Goldsmith, P. F. 1996, ApJ, 460, 343
Boger, G. I., & Sternberg, A. 2005, ApJ, 632, 302
Brogan, C. L., & Troland, T. H. 2001, ApJ, 560, 821
Cabrit, S. 2007, LNP, 723, 21
Cesaroni, R., & Walmsley, C. M. 1991, A&A, 241, 537
Crutcher, R. M. 2004, Ap&SS, 292, 225
Crutcher, R. M. 2007, in Sky Polarisation at Far-Infrared to Radio Wavelengths: The Galactic Screen before the Cosmic Microwave Background, ed. M.-A. Miville-Deschênes, & F. Boulanger, EAS Publication Series, 23, 37
Crutcher, R. M., Troland, T., Lazareff, B., & Kazès, I. 1996, ApJ, 456, 217
Crutcher, R. M., Troland, T., Lazareff, B., Paubert, G., & Kazès, I. 1999, ApJ, 514, L121
Güsten, R., Fiebig, D., & Uchida, K. I. 1994, A&A, 286, L51
Heiles, C., & Troland, T. H. 2005, ApJ, 624, 773
Hily-Blant, P., Walmsley, M., Pineau des Forêts, G., & Flower, D. 2008, A&A, 480, L5
Ho, P. T. P., Terebey, S., & Turner, J. L. 1994, ApJ, 423, 320
Johnstone, D., Boonman, A. M. S., & van Dishoeck, E. F. 2003, A&A, 412, 157
Kim, S.-J., Kim, H.-D., Lee, Y., et al. 2006, ApJS, 162, 161
Lada, E. A., Evans, N. J., II, & Falgarone, E. 1997, ApJ, 488, 286
MacLow, M.-M., & Klessen, R. S. 2004, Rev. Mod. Phys., 76, 125
Minchin, N. R., Ward-Thompson, D., & White, G. J. 1995, A&A, 298, 894
Minier, V., Burton, M. G., Hill, T., et al. 2005, A&A, 429, 945
Mouschovias, T. Ch., & Ciolek, G. E. 1999, in The Origin of Stars and Planetary Systems, ed. C. J. Lada, & N. D. Kylafis (Kluwer), 305
Mueller, K. E., Shirley, Y. L., Evans, N. J., II, & Jacobson, H. R. 2002, ApJS, 143, 469
Omodaka, T., Kobayashi, H., Kitamura, Y., Nakano, M., & Ishiguro, M. 1992, PASJ, 44, 447
Padin, S., Sargent, A. I., Mundy, L. G., et al. 1989, ApJ, 337, L45
Plume, R., Jaffe, D. T., Evans, N. J., II, Martin-Pintado, J., & Gomez-Gonzalez, J. 1997, ApJ, 476, 730
Reid, M. J., Xu, Y., Zheng, X. W., & Menten, K. M. 2005, A&AS, 207, 4006
Schneider, N., Simon, R., Bontemps, S., Comerón, F., & Motte, F. 2007, A&A, 474, 873
Shu, F., Allen, A., Shang, H., Ostriker, E. C., & Li, Z.-Y. 1999, in The Origin of Stars and Planetary Systems, ed. C. J. Lada, & N. D. Kylafis (Kluwer Academic Publishers), 193
Simon, R. 1998, private communication
Tatematsu, E., Umemoto, T., Kameya, O., et al. 1993, ApJ, 404, 643
Turner, B. E., & Gammon, R. H. 1975, ApJ, 198, 71
Uchida, K.I., Fiebig, D., & Güsten, R. 2001, A&A, 371, 274
Vallée, J. P., & Fiege, D. 2005, ApJ, 627, 263
Vallée, J. P., & Fiege, D. 2006, ApJ, 636, 332
Wang, Y., Jaffe, D. T., Evans, N. J., II, et al. 1993, ApJ, 419, 707
Zhou, S., Butner, H. M., Evans, N. J., II, et al. 2004, ApJ, 428, 219